The Journal of Chemical Physics

RESEARCH ARTICLE | JUNE 24 2026

Exploring nanographene for single molecule imaging at cryogenic temperatures

Yutong Wang ; Qiqi Yang; Xiaomin Liu ; Sjoerd Stallinga ; Bernd Rieger

J. Chem. Phys. 164, 244201 (2026)
https://doi.org/10.1063/5.0327382

The Journal of Chemical Physics ARTICLE pubs.aip.org/aip/jcp

Exploring nanographene for single molecule imaging at cryogenic temperatures

Cite as: J. Chem. Phys. 164, 244201 (2026); doi: 10.1063/5.0327382
Submitted: 11 February 2026 • Accepted: 27 April 2026 •
Published Online: 24 June 2026

Yutong Wang,[1] Qiqi Yang,[2] Xiaomin Liu,[2] Sjoerd Stallinga,[1] and Bernd Rieger[1,a)]

AFFILIATIONS

[1] Department of Imaging Physics, Delft University of Technology, Delft, The Netherlands
[2] Max Planck Institute for Polymer Research, Mainz, Germany

[a)] **Author to whom correspondence should be addressed:** b.rieger@tudelft.nl

ABSTRACT

Imaging single fluorescent molecules at cryogenic temperatures can increase photon budgets by suppressing photobleaching and non-radiative loss. Combined with rapid-freezing vitrification, it enables correlative cryo-fluorescence and electron microscopy. Obtaining a wide set of fluorophores with suitable blinking characteristics at cryogenic temperatures has remained a challenge. Nanographenes are self-blinking fluorophores that could fill this gap, yet their low-temperature intermittency remains largely unquantified. Here, we characterize the blinking and photon output of single dibenzo[hi,st]ovalene (DBOV-azide) nanographene fluorophores on glass from 91 to 293 K over excitation irradiances of 1.2–5.9 kW cm^{-2}. On/off fluorescence states are extracted from wide-field images using a generalized likelihood ratio test, with simulation-based validation to reduce false detections under high-background conditions. We find that DBOV-azide blinks at all temperatures, with mean on-times that decrease with increasing temperature (longer at 91 K than at room temperature) and that further shorten with increasing irradiance at 91 K. For short time scales ($t < 1.5$ s), on- and off-time distributions follow power laws with exponents −1.6 to −1.2 that show no systematic dependence on temperature or irradiance. The mean on/off ratio drops by ~10× from 91 to 293 K, indicating a worse duty cycle at lower temperature. Photon output increases with irradiance and is higher at cryogenic temperatures, with an order-of-magnitude increase in photons per on-event compared to room temperature.

I. INTRODUCTION

Super-resolution fluorescence microscopy circumvents the diffraction limit to reveal nanoscale structures in cells and materials. Among the many existing modalities, single-molecule localization microscopy (SMLM) is widely used and achieves nanometer-scale precision by localizing emitters that are spatially and temporally isolated. This separation can be achieved either by activation of photoactivatable/photoconvertible fluorophores in photoactivated localization microscopy (PALM), typically using ultraviolet or violet activation light,[1,2] or by stochastic optical reconstruction microscopy (STORM) where the fluorophores blink stochastically due to the presence of a suitable liquid buffer that facilitates redox reactions of the fluorophores.[3,4] Only if this separation results in such a spare image that, on average, only one fluorophore emits light in a diffraction-limited area, the center of the emission can be pinpointed with nanometer precision. The achievable localization precision obtained by fitting observed single-molecule spots with a point-spread function (PSF) model improves with the number of detected photons.[5] Long-time acquisition at room temperature, however, is limited by photobleaching, which caps the number of foreground photons per fluorescent molecule. These constraints motivate operating conditions that deliver higher photon budgets emitted from single emitters.

Cryogenic fluorescence microscopy addresses this bottleneck. Cooling to liquid-nitrogen temperatures (~77 K) suppresses many non-radiative and photobleaching processes, so that individual fluorophores can emit orders of magnitude more photons and can be localized with sub-nanometer precision in favorable cases.[6–9] Experiments on a variety of organic dyes and fluorescent proteins have demonstrated photon yield enhancements of one to several orders of magnitude at cryogenic temperature compared to room temperature, directly translating into improved localization precision for single-molecule imaging.[8,10]

At the same time, rapid freezing preserves the ultrastructure of biological samples close to their native state and avoids many artifacts of chemical fixation.[11,12] This vitrification results in an amorphous ice state, which is important as this state of ice is transparent to high-energy electrons for later correlative imaging. Cryogenic light microscopy, therefore, offers the exciting opportunity to be combined with cryo-electron microscopy (cryo-EM) in correlative workflows, where fluorescence microscopy provides molecular specificity and cryo-EM provides structural context at nanometer or even sub-nanometer resolution.[10,13] Early studies showed that standard or photoactivatable fluorescent proteins can support super-resolution imaging at cryogenic temperatures in cells and can be correlated with three-dimensional cryo-EM.[14–17] More recently, integrated instruments that combine simultaneous and coincident cryogenic imaging with electron and photon beams, together with fluorescence-guided lamella milling with ion beams, have turned cryo-compatible fluorescence microscopy into a practical tool for targeting regions of interest for high-resolution cryogenic electron tomography (cryo-ET).[18,19]

A variety of complementary strategies have been developed to realize single-molecule localization microscopy at cryogenic temperatures. One line of work uses fluorescent proteins that retain photoactivation or photoswitching at low temperature.[14,15,17,20,21] Correlated cryogenic super-resolution fluorescence microscopy and cryo-ET on bacterial and mammalian cells have shown that photoactivatable or photoswitchable fluorescent proteins can be switched and localized at liquid-nitrogen temperatures.[14,15,17] These studies demonstrated that a subset of fluorescent proteins that can be used at room temperature remains partly switchable at cryogenic temperatures to support single-molecule localization of cellular ultrastructure.[8–10] Photophysics at low temperatures differs from that at room temperature because freezing changes lifetimes and photoswitching kinetics. As a result, illumination schemes and exposure times need to be adjusted under cryogenic conditions to the best possible on–off duty cycle and photon budget for single-molecule imaging.[8,10,20] In particular, mApple and PAmKate have been characterized in detail at low temperature, revealing distinct emissive and non-emissive states and establishing two-color illumination schemes [typically 405 nm light for (re)activation and a longer-wavelength light in the green–red range for readout] that provide active control over on- and off-states.[20,21] These fluorescent proteins offer biological workflows for cryo-PALM and cryo-SMLM, but in practice, they still require tuning of activation and illumination intensities to balance sparsity, brightness, and photostability at cryogenic temperatures, while the achievable sparsity is poorer compared to room temperature.

A second line of work exploits the fixed dipole orientation of emitters at cryogenic temperatures. Upon vitrification, emitters are immobilized and can no longer reorient freely during the camera exposure. Each fluorophore behaves as a fixed dipole, which introduces strong polarization dependence in excitation and detection and, under high numerical aperture conditions, leads to anisotropic and orientation-dependent emission PSF. These effects need to be taken into account in the PSF model used for fitting and in the detection strategy for single-molecule analysis, but they can also be exploited as an additional contrast mechanism. Polarization-selective excitation and depletion have been proposed as ways to select subsets of emitters and thereby induce sparsity for localization microscopy at cryogenic temperatures.[22,23] Related approaches use polarization-encoded detection to distinguish differently oriented dipoles within one diffraction-limited spot and achieve multi-target colocalization with Ångström-level relative precision.[24,25]

Beyond protein-based fluorophore choice and polarization control, optical architectures can also be adapted to cryogenic conditions. Waveguide-based cryogenic total internal reflection fluorescence microscopy exploits guided optical modes in photonic chips to generate an evanescent field over comparatively large fields of view, providing near-membrane excitation with strong background suppression and benefiting from the increased photo-stability of fluorophores at low temperature.[26]

Finally, there is growing interest in non-protein fluorophores whose native photophysics at low temperature already provide intermittent emission without the need for special switching buffers or photoactivation. Among these, intrinsically blinking nanographene dibenzo[hi,st]ovalene (DBOV) has been shown to exhibit high brightness, photo-stability, and burst-like blinking at room temperature, supporting super-resolution imaging in solution and in cells.[27–29] These properties suggest that such labels could offer a relatively straightforward route toward cryo-compatible SMLM. Their blinking statistics at cryogenic temperatures, however, remain largely unexplored.

Here, we investigate nanographene DBOV-azide as a representative intrinsically blinking fluorophore because of its compact size and red emission compatible with standard fluorescence imaging. We explore its potential as a spontaneously blinking fluorophore for cryo-SMLM at a ~90–100 K temperature range by addressing two questions: (i) What on–off ratio does DBOV exhibit at cryogenic temperature, defined as ratio of the average emissive ("on") time t_{on} to the average non-emissive ("off") time t_{off}? We investigate whether this level is sufficient for SMLM under typical fluorophore sparsity, noting that lower duty cycles permit proportionally more molecules to be localized within a diffraction-limited area and, therefore, support higher labeling densities before PSF overlap limits resolution. (ii) How does the on–off ratio vary with temperature and excitation intensity?

To this end, we investigate DBOV near liquid-nitrogen temperature (91 K) and above using a wide-field, cryo-compatible fluorescence microscope introduced previously.[22] We record single-emitter time traces across a range of temperatures and excitation intensities. On and off states are classified in each time trace, and the on- and off-time (t_{on}, t_{off}) distributions and photon yields are quantified to characterize the blinking statistics of DBOV.

This paper is organized as follows: Sec. II details the sample preparation, cryogenic imaging setup, data acquisition, and fluorescence time trace analysis. Section III reports the on- and off-time distributions and photon output, and quantifies their temperature- and excitation-dependent statistics. Section IV provides interpretation and connection to prior literature on nanographene blinking mechanisms, summarizes practical operating windows for DBOV at cryogenic temperatures, and outlines an outlook for cryo-SMLM using intrinsically blinking nanographenes.

II. METHOD

A. DBOV-azide molecule

DBOV-azide is a functionalized nanographene derived from a dibenzo[hi,st]ovalene (DBOV) core that carries three triethyleneglycol side chains for aqueous compatibility and a terminal azide group for bioorthogonal copper-catalyzed azide–alkyne cycloaddition (CuAAC; "click labeling").[29] The synthesis of the compound and complete characterization by nuclear magnetic resonance spectroscopy and high-resolution mass spectrometry are reported by Zhu *et al.*[29] The DBOV core has been reported to exhibit red emission with a high quantum yield of ~80%. In our microscope setup, excitation and detection wavelengths follow the ranges reported for DBOV derivatives (see Fig. 1), that is, red excitation (e.g., 633–642 nm) and emission collection in the 660–760 nm window. At the single-molecule level, DBOV-azide displays intrinsic burst-blinking under red excitation. For biological conjugation, the azide handle was used for CuAAC labeling of O-propargyl-puromycin-tagged nascent polypeptides in neurons.

B. Sample preparation

1. Reagents and materials

The following reagents and materials were used for sample preparation: anhydrous toluene (≥99.8%); 2% v/v Hellmanex™ III detergent; acetone; isopropanol; 12 mm diameter, thickness No. 1.5H high-precision cover glasses (Marienfeld, Catalog No. 0117520); and glass syringes.

2. Coverslip cleaning

Coverslips were cleaned as follows: (i) sonicated 15 min in 2% Hellmanex solution; (ii) rinsed thoroughly with Milli-Q water (three times); (iii) sonicated 15 min in acetone (or 5 min Milli-Q + 10 min isopropanol); (iv) dried with nitrogen; and (v) oxygen-plasma cleaned immediately before use (200–300 W, 5–10 min). Cleaned substrates were kept in a dust-free container until deposition.

3. Cleaning of vials, caps, and syringes

Glass vials were cleaned identically to coverslips. Polytetrafluoroethylene (PTFE)-lined caps were soaked 15 min in Milli-Q water, sonicated 15 min in 2% Hellmanex, rinsed three times with Milli-Q, and dried with nitrogen. Glass syringes were rinsed sequentially with acetone (or isopropanol), 2% Hellmanex, Milli-Q water, and acetone and then dried with nitrogen and stored sealed.

4. DBOV-azide stock and serial dilution in toluene

A DBOV-azide stock (10^{-4}M in toluene) was prepared in a cleaned glass vial. Serial 1:100 dilutions were made to 10^{-6}, 10^{-8}, 10^{-10}, and 10^{-12}M by transferring 10 μl of the higher-concentration solution into 990 μl toluene and vortexing for ≥30 s at each step. All solutions were stored upright in capped glass vials, protected from dust and light.

5. Deposition and spin-coating for sparse single-molecule samples

Freshly plasma-cleaned coverslips received 10 μl of the 10^{-12}M DBOV-azide solution in toluene and were spin-coated at 2000 rpm for 60 s (typical acceleration 500–1000 rpm s^{-1}). These conditions reproducibly yielded isolated emitters suitable for single-molecule measurements. If necessary, the surface density was tuned by adjusting the working concentration (10^{-11}–10^{-13}M), dispense volume (5–20 μl), or spin speed (1000–3000 rpm).

6. Handling and storage

Prepared samples were stored in a clean, dry, dust-free container and kept protected from light. Contact with polymeric plastics was minimized to avoid leaching of contaminants or adsorption of residues onto the sample surface.

C. Cryo fluorescence microscope setup

A custom-built wide-field fluorescence microscope adapted from our earlier work[22,23] was used for cryogenic single-molecule imaging (Fig. 2). Excitation was provided by a 642 nm fiber laser (2RU-VFL-P-2000-642-B1R, MPB Communications). The laser output was spatially filtered and expanded 5× by a telescope comprising a focal length of 30 mm focal-length achromatic doublet (AC254-030-A, Thorlabs), a 40 μm pinhole at the intermediate focus (P40K, Thorlabs), and a 150 mm focal-length plano-convex lens (LA1433-A, Thorlabs), increasing the beam diameter from 0.5 to 2.5 mm. After a steering mirror (M; PF10-03-P01 protected silver,

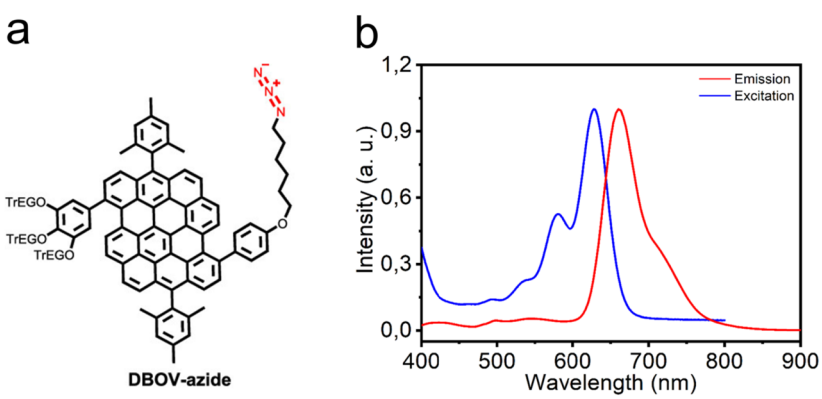

FIG. 1. (a): Chemical structure of DBOV-azide, adapted from Zhu *et al.*, J. Am. Chem. Soc. **146**(8), 5195–5203 (2024), licensed under a Creative Commons Attribution (CC BY 4.0) license. (b): Representative absorption and emission spectra for DBOV derivatives in the red channel (data/conditions are the same as in the work by Zhu *et al.*[29]).

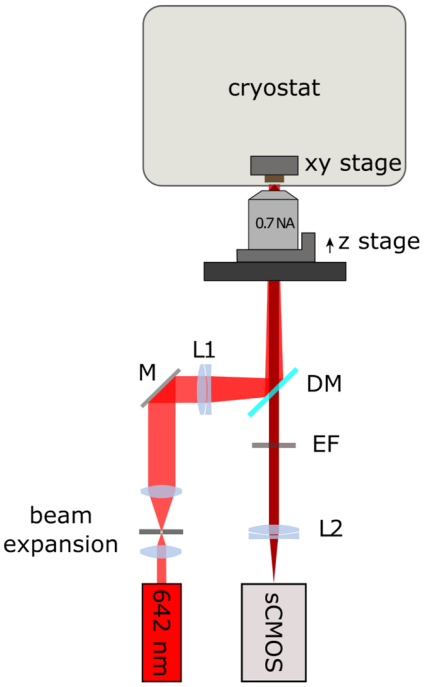

FIG. 2. Schematic of the experimental setup. Component labels (M, L1, DM, EF, and L2) are further described in the main text.

Thorlabs), an achromatic excitation relay lens (L1; AC254-150-A, f = 150 mm, Thorlabs) imaged the beam onto the back focal plane of the objective, establishing a 4f configuration and producing a weakly converging Gaussian illumination at the specimen. A dichroic beam splitter (DM; FF652-Di01-25 × 36, Semrock) was used to direct the excitation into the objective.

Fluorescence was collected by a 60×/0.70 NA air objective with an extended working distance (CFI S Plan Fluor ELWD 60XC, Nikon). The long working distance (1.8–2.6 mm) enabled the objective to remain outside the cryostat, while the sample, prepared on a No. 1.5H high-precision glass coverslip with a 12 mm diameter, was cooled inside. Axial focusing was provided by a piezo-driven linear stage beneath the objective (Q-545 Q-Motion, Physik Instrumente), and lateral positioning of the sample was achieved with two orthogonally stacked piezoelectric linear stages inside the cryostat (Q-545.140, Physik Instrumente; 13 mm travel, 1 nm resolution). Emission light passed through the cryostat window of 500 μm thick fused-quartz, and then through the dichroic and two stacked bandpass filters centered at 676 nm with 29 nm FWHM (EF; FF01-676/29-25, Semrock).

The image was formed by a tube lens (L2; ITL200, f = 200 mm, Thorlabs) onto a scientific CMOS camera (Zyla 4.2 PLUS, Andor). Component labels (M, L1, DM, EF, and L2) correspond to those indicated in Fig. 2.

D. Cryostat and vacuum operation

Cryogenic imaging was performed in a customized liquid-nitrogen cryostat operated under high vacuum. The sample holder inside the vacuum chamber was thermally linked to a liquid-nitrogen (LN_2) reservoir via copper heat conductors, while the heat conductor, LN_2 tank, and sample stage were enclosed in vacuum to suppress convective heat transfer. In routine operation, we first pumped the chamber to $\leq 5 \times 10^{-5}$ mbar and then filled the cryostat with LN_2. The sample temperature stabilized after ~1 h.[23]

Under steady-state cryogenic conditions, the sample-stage temperature was $T_s \approx 90.5$ K, with a stability of ±0.17 K over 30 h and an average slope of ~0.04 K h^{-1} (maximum ~0.13 K h^{-1}). Lateral drift was ~0.8 μm over 3 h, while axial drift was slightly larger (~1.6 μm/3 h); most drift occurred within the first 20 min after turning on the excitation light. In our acquisitions at 91 K, we, therefore, performed periodic refocusing during a typical 800 s measurement window to compensate residual z-drift (see Subsection II E).

After all LN_2 had evaporated, the sample warmed slowly at ~18.5 K h^{-1} (≈0.31 K min^{-1}). We exploited this gradual warm-up to record data at intermediate temperatures (100, 150, 200, 250, and 282 K). Over a single 800 s time trace, T_s increased by only ~4.1 K, which was small compared to our 50 K temperature spacing; thus, we treated T_s as quasi-stationary within each acquisition while compensating the increased z-drift by refocusing approximately every 2 min (see Subsection II E).

Further engineering details of the cryostat design, sensor and pump configuration, and a full performance characterization (temperature time courses and 3D drift) are provided in Ref. 23.

E. Image acquisition

1. Excitation and irradiance

The 642 nm laser was operated in a continuous-wave mode. We used six measured laser output powers {219, 327, 473, 600, 800, 1064 mW}, corresponding to irradiances of {1.2, 1.9, 2.7, 3.3, 4.6, 5.9} kW cm^{-2} on the sample plane, respectively. The laser irradiances on the sample plane were calculated from the measured excitation-path transmission and the 1/e^2 beam diameter of 173.4 μm from the acquired laser beam profile at the sample plane.

2. Camera settings

Images were recorded with a scientific CMOS camera (Zyla 4.2 PLUS, Andor) using a 400 × 400 pixel region of interest, corresponding to a 43.3 × 43.3 μm field of view (FOV) in the sample plane (effective sampling ≈108 nm/pixel), centered on the illuminated area. The camera was operated with 12-bit dynamic range and the 200 MHz (lowest-noise) readout mode. The exposure time was 40 ms, and each acquisition stack contained 20 000 frames (total duration 800 s). The sensor temperature was stabilized at 0 °C.

3. Temperature and drift handling

Intermediate-temperature datasets were acquired during the gradual warm-up after LN_2 depletion (rate ~0.24 K min^{-1}), while 91 and 293 K datasets were recorded at steady temperature. Residual axial drift was mitigated by brief manual refocusing: approximately every 5 min at 91 K and every 2 min during warm-up, where z-drift was dominant. The initial ~10 s of frames collected during stage refocusing at the start of acquisition were discarded prior to time-trace analysis.

4. Field selection and start-of-illumination capture

To consistently capture the moment immediately after the excitation was turned on, coarse focusing was performed in a nearby area (within the same coverslip region) to avoid premature photobleaching at the target FOV. We then translated to the target FOV, performed fine focusing (a few seconds), and started the acquisition. Each dataset was recorded at a fresh FOV to avoid history effects.

F. Data analysis

All analyses were performed in MATLAB (R2025a, MathWorks) using custom scripts based on the open-source DIPimage image-analysis toolbox (DIPimage v3.2.0; diplib.org). The software developed in this work is openly available in a public GitLab repository.[30] The processing and analysis steps were as follows.

1. Image pre-processing and segmentation into ROIs

Raw camera image stacks (400 × 400 pixels, 20 000 frames, 16-bit TIFF) were imported. Pixel values in analog-to-digital units (ADU) were converted to detected photon counts using camera calibration (offset subtraction and gain correction),[31] and the estimated offset was 102.3 ADU and gain was 0.3 e^-/ADU. A maximum-intensity projection over all time frames was computed to locate candidate emitters by local-maximum detection in this projected image. Local maxima are found by a difference of uniform filters with different sizes, similar to those in Ref. 32. For each candidate, we defined a square ROI whose width covers $\sim\pm 3\sigma_{\mathrm{PSF}}$ to all sides of the peak. In pixels, we used the ROI size $d_{\mathrm{ROI}} = 2 \times 3\sigma_{\mathrm{PSF}} + 1$, ensuring an odd width and full PSF support for the fitting.[32] The PSF size was taken to be $\sigma_{\mathrm{PSF}} = \lambda/4\mathrm{NA}$ as the best fit to a Gaussian model.[33] ROIs containing multiple nearby peaks and those with overlaps or neighbors within $d_{\min} = d_{\mathrm{ROI}} - 2$ were excluded so that each ROI contained a single emitter for downstream analysis.

2. On–off detection by a generalized likelihood ratio test

Segmenting fluorescence time traces into on/off states is non-trivial in our cryogenic wide-field recordings. First, the reflective metal sample holder produces a relatively high, condition-dependent background (typically tens of photons per pixel per frame), which varies across ROIs and with experimental settings. Second, many emitters blink sparsely or dimly. The on-states can last only a few frames, and the on-state signal may be only slightly above background. As a result, the photon count histogram of a single trace often lacks clear separation between on- and off-level intensity distributions, and a global, fixed threshold is unreliable across datasets.

We explored several commonly used on/off detection methods on our data and found them insufficient to meet our requirements for high reliability, single-frame time resolution, and robustness to varying backgrounds. (i) Intensity-threshold methods, including fixed thresholds based on background fluctuations or photon count histogram-based thresholds, are widely used for blinking analysis.[34–37] However, in our low signal-to-background ratio (SBR) traces, the threshold choice becomes ambiguous and can artificially fragment a continuous on-state into multiple short on/off switches, thereby biasing on/off time statistics. (ii) Change-point analysis methods on intensity time traces, implemented with Bayesian statistics to identify jumps or change points in traces,[38–41] tend to be less sensitive to short events that occupy only a few frames and require selecting priors, such as the number of signal steps and transition rates, which are not known for our data. Moreover, operating purely on summed intensity discards spatial information that helps distinguish a true PSF-shaped signal from fluctuations or imaging artifacts. (iii) Standard SMLM data processing pipelines are optimized for accurate emitter localization rather than per-frame state determination and thus, may miss dim on-frames or split on-periods under low SBR.[32]

These considerations motivate an imaging-model-based, per-frame detector that uses the full ROI image of a single emitter rather than a 1D intensity trace, explicitly models the foreground and background under the realistic PSF and noise model, and can detect short on-events without relying on heuristic thresholds. We, therefore, use a generalized likelihood ratio test (GLRT), which compares a background-only model with an emitter-plus-background model, together with false discovery rate thresholding to control false positives.[42]

This method is based on evaluating the relative likelihood of two hypotheses: the background-only model $H_0: \mu_{ij} = I_{\mathrm{bg}}$ and the emitter-plus-background model $H_1: \mu_{ij} = I_{\mathrm{bg}} + I_0 G_{ij}$. Here, i,j are the ROI image pixel indices; I_{bg} is a spatially constant background within the ROI; I_0 is the emitter strength; and G_{ij} represents the pixel-integrated weights of a unit-normalized 2D Gaussian PSF as in Ref. 32. Under the Poisson noise model, with n_{ij} being the observed photon counts in pixel (i,j) of an ROI frame, the log-likelihoods are

$$\log \mathscr{L}(H_0) = \sum_{ij} \left[n_{ij} \log I_{\mathrm{bg}} - I_{\mathrm{bg}} \right] + \text{const},$$

$$\log \mathscr{L}(H_1) = \sum_{ij} \left[n_{ij} \log \left(I_{\mathrm{bg}} + I_0 G_{ij} \right) - \left(I_{\mathrm{bg}} + I_0 G_{ij} \right) \right] + \text{const}.$$

We obtain the maximum-likelihood estimates $\hat{I}_{\mathrm{bg}}^{(0)}$ (under H_0) and $(\hat{I}_{\mathrm{bg}}^{(1)}, \hat{I}_0)$ (under H_1) by maximizing the above-mentioned expressions.

In the estimate under H_1, we use a simplified route to estimate the position of the emitter due to the large number of required fits and as we do not care about the exact position after all. Instead of fitting the position in each frame independently, we estimate the center position once on the maximum intensity projection using the phasor approach by Ref. 43. This position is then used in the hypothesis test H_1 for all frames in this ROI. This restriction is acceptable as (i) the samples are static and (ii) the actual position with nanometer precision is not relevant here, but is only to detect whether the emitter is in the on-state. As the GRLT computation needs to be computed per frame for very many frames for each ROI, this simplified procedure offers a significant computational gain. The estimation of the foreground photon count under hypothesis H_1 is done with a fixed constant PSF width $\sigma_{\mathrm{PSF}} = \lambda/4\mathrm{NA}$. Gaussian fitting is known to give an underestimation of the actual photon count (compared to, e.g., vectorial PSF fitting) of 10%–20%.[44] This underestimation is not critical here as only the classification into on and off states is needed.

From the two likelihood values, we compute the log-likelihood ratio test statistic,

$$\mathrm{LLR} = 2(\log \mathscr{L}(H_1) - \log \mathscr{L}(H_0)) \geq 0.$$

For decision making, we convert LLR to a per-frame false positive probability as

$$p = 2\,\mathrm{CDF}\left(-\sqrt{LLR}\right), \tag{1}$$

where

$$\mathrm{CDF}(x) = \frac{1}{2}\left[1 + \mathrm{erf}\left(\frac{x}{\sqrt{2}}\right)\right]$$

denotes the standard normal cumulative distribution function and erf is the Gaussian error function. The collection of per-frame p-values within a trace is then thresholded by the Benjamini–Yekutieli false discovery rate (FDR) procedure with parameter q.[45] Given m framewise tests with p-values from Eq. (1), sort them as $p_{(1)} \leq \cdots \leq p_{(m)}$ and find the largest k satisfying

$$p_{(k)} \leq \frac{q\,k}{m\,c(m)}, \qquad c(m) = \sum_{i=1}^{m} \frac{1}{i}.$$

Set the global threshold $p_{\mathrm{th}} = p_{(k)}$ and label frames with $p_{(i)} \leq p_{\mathrm{th}}$ as "on" (else "off"). We used the FDR control parameter $q = 0.03$ in all analyses.

3. Quality control and false-positive mitigation

The GRLT can detect very weak signals over the background. Unfortunately, we found that it is quite sensitive and can still yield a noticeable number of false-positive (FP) detections with very weak signal photon counts, particularly at low SBR. Adjusting the GLRT FDR q alone appears to be insufficient. Lowering q to suppress these weak-signal FPs also progressively discards genuine on frames (i.e., increases false negatives), and this effect becomes apparent for $q < 10^{-2}$. We, therefore, set $q = 0.03$ to preserve sensitivity and applied an additional post-filtering step to remove only the residual weak-signal detections that are most likely false positives. This post-filtering step is based on a background adaptive thresholding that is calibrated from a simulation study. We simulated blinking emitters for different foreground (100–1500 in steps of 50 photons) and background values (5–80 photons per pixel in steps of 5) with the same settings as the actual experiment. From the comparison of the simulation outcome to the known ground truth, we computed the Matthews correlation coefficient (MCC),

$$MCC = \frac{TP \cdot TN - FP \cdot FN}{\sqrt{(TP+FP)(TP+FN)(TN+FP)(TN+FN)}},$$

a standard measure of binary classification performance.[46] Here, the different symbols are TP, the number of true positives; TN, the number of true negatives; FP, the number of false positives; and FN, the number of false negatives. For a coefficient $MCC \geq 0.95$, we set a threshold for the minimal foreground intensity I_{min} needed, given a certain background value in the experiment (see Fig. 3). We can fit a line to the boundary values,

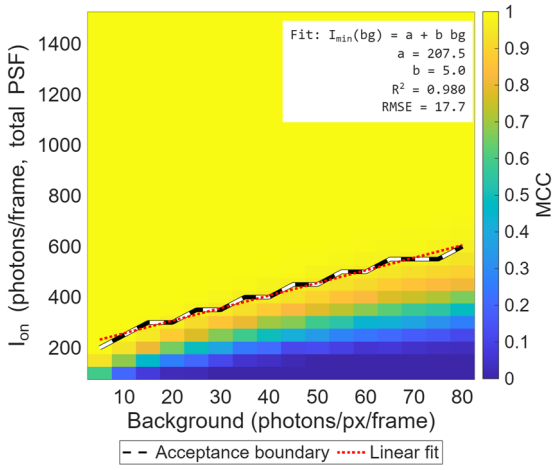

FIG. 3. SBR-dependent acceptance threshold. The heat map shows GLRT performance quantified by the MCC over a grid of foreground and background levels: $I_{\mathrm{on}} = 100 : 50 : 1500$ photons/frame (total PSF) and $bg = 5 : 5 : 80$ photons/pixel/frame. The dashed curve marks the acceptance boundary, i.e., the minimal I_{on} for each background level that achieves $MCC \geq 0.95$. The red dotted line is a linear least-squares fit to the boundary points, $I_{\mathrm{min}}(bg) = a + b\,bg$ (photons/pixel/frame), yielding $a = 207.5$ and $b = 5.0$.

$$I_{\mathrm{min}}(bg) = a + b \cdot bg,$$

which for our experiments was $I_{\mathrm{min}}(bg) = 207.5 + 5.0 \times bg$ (photons/frame). We used this to post-filter found "on" frames, keeping only those with $I_{\mathrm{on}} \geq I_{\mathrm{min}}(bg)$.

To apply the background-adaptive acceptance threshold $I_{\mathrm{min}}(bg)$ to real data, the per-pixel background bg was computed as the mean over all fitted background values under the background-only model (H_0) per trace, representing a single blinking molecule. The adaptive threshold $I_{\mathrm{min}}(bg)$ was then applied individually to each trace during post-filtering. Only "on" frames with the estimated foreground counts exceeding $I_{\mathrm{min}}(bg)$ were retained. Finally, on and off intervals that touch the first or last frame of the recording are excluded from on/off-time and photon count statistics, as their actual duration cannot be measured.

4. Blinking statistics

From the on–off detection, we extracted on- and off-time durations $t_{\mathrm{on}}^{(i,k)}$ and $t_{\mathrm{off}}^{(i,k)}$ for every event k of every emitter i detected in the field of view. From this data, we computed two different averages. The event-pooled mean, $\langle t_{\mathrm{on}} \rangle_{\mathrm{events}}$ and $\langle t_{\mathrm{off}} \rangle_{\mathrm{events}}$, pools all events across emitters so that each event has equal weight. The per-emitter mean (mean-of-means) first averages the data for each emitter, $\bar{t}_{\mathrm{on}}^{(i)}$ and $\bar{t}_{\mathrm{off}}^{(i)}$, and then averages these across emitters, yielding $\langle \bar{t}_{\mathrm{on}} \rangle_{\mathrm{emitters}}$ and $\langle \bar{t}_{\mathrm{off}} \rangle_{\mathrm{emitters}}$, so each emitter has equal weight. We also computed two on–off ratios as ratios of means: the event-pooled ratio $r_{\mathrm{events}} = \langle t_{\mathrm{on}} \rangle_{\mathrm{events}} / \langle t_{\mathrm{off}} \rangle_{\mathrm{events}}$ and the per-emitter ratio $r_{\mathrm{emitters}} = \langle \bar{t}_{\mathrm{on}} \rangle_{\mathrm{emitters}} / \langle \bar{t}_{\mathrm{off}} \rangle_{\mathrm{emitters}}$.

For visualization of the t_{on} and t_{off} distributions, we plot counts on a double logarithmic scale (log–log display) and fit the distributions with a power law,

$$P(t) = B\,t^{\alpha}, \tag{2}$$

where $P(t)$ is the normalized probability density, B is a scaling prefactor, t is the time (either t_{on} or t_{off}), and α is the power-law exponent. Power-law fits were applied to bins with at least five counts and weighted by counts to suppress events in the long tail of the distributions. Because the on- and off-time distributions are non-Gaussian and heavy-tailed, means and standard errors (SEs) of t_{on} and t_{off} were obtained by nonparametric bootstrap resampling: for each dataset, we generated 10 000 same-size resamples by sampling times with replacement, computed the mean for each resample, and took the SE as the standard deviation of the bootstrap means.[47] In addition, we computed per-frame and per-on-event (sum over an on state) foreground and background photon counts. Means and SEs for the foreground photon counts were estimated by bootstrap resampling in the same way.

The determination of power-law blinking parameters is known to be susceptible to biases arising from thresholding procedures.[48,49] We expect that our combination of an image-based GLRT that avoids an ad hoc intensity threshold, together with a physically motivated, background-adaptive post-selection to remove residual low-SBR false positives, will mitigate these biases.

III. RESULTS

A. Single DBOV molecules blink at cryogenic temperature

Figure 4(a) shows a sparse wide-field image of single DBOV-azide emitters recorded at 91 K (intensity in photons per camera frame, frame time 40 ms). Isolated diffraction-limited spots are visible over the flat background. The time trace from the boxed emitter exhibits intermittent emission, with contiguous emissive (on) states separated by dark (off) intervals. At 91 K, an on state typically spans multiple camera frames, whereas at 293 K, on states are generally shorter (see the traces in Fig. 5). A video recording of the same FOV at 91 K further illustrates the fluorescence blinking behavior shown in Fig. 4(a) (Multimedia available online).

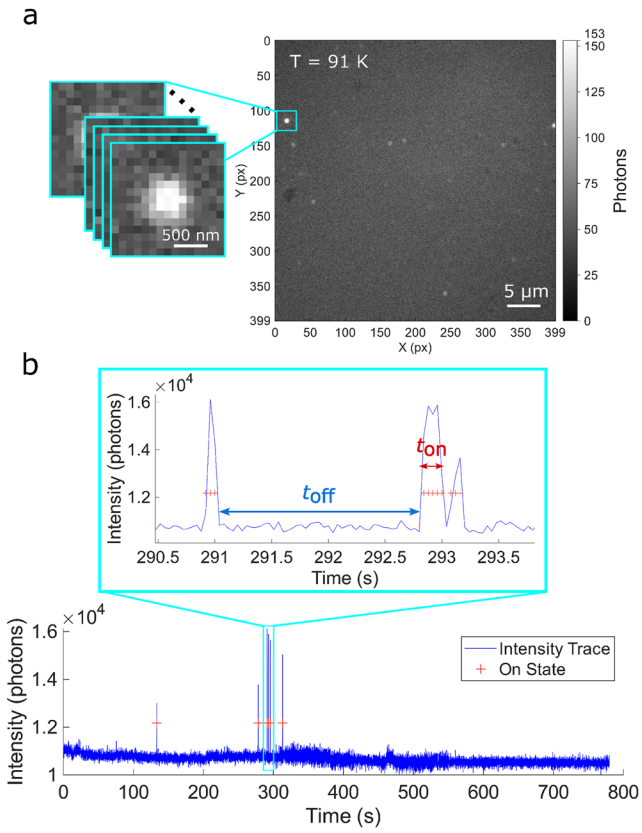

FIG. 4. (a) Example of a single frame from a time-series fluorescence recording of sparse nanographene at 91 K. The image is displayed linearly from 0 to 153 photons (99.99th percentile of pixel values in the image) to enhance visibility. (b) Intensity trace for the boxed emitter in panel (a). The red crosses mark the frames classified as on frames by the GLRT. A 60 s video recording of the field of view shown in panel (a) is available online (Multimedia available online).

B. Representative blinking behavior for different temperatures

Figure 5 presents nine representative intensity traces of individual DBOV-azide molecules acquired at the same irradiance at temperatures 91, 200, and 293 K. At 91 K [(a)–(c)], molecules exhibit intermittent emission with on states that typically last several frames of 40 ms. In some traces (a), the bursts rise well above background with occasional high spikes, whereas in others [(b), (c)] the signal remains elevated for extended periods, showing either frame-to-frame fluctuations that indicate frequent switching events or extended intervals in a sustained on state rather than isolated spikes. At 200 K [(d)–(f)], the traces remain intermittent and show a transitional behavior between 91 and 293 K. On states are shorter and more separated than at 91 K, but longer on-state intervals still occur more often than spike-like traces at 293 K. At 293 K [(g)–(i)], on states are predominantly short and are punctuated by frequent returns to the background level. The three example types (sparse, frequent, and intermediate on–off switching) span the range of blinking behaviors observed across all temperatures in the dataset. Overall, the on-state duration is longer and per-frame photon fluctuations are more pronounced at cryogenic temperature than at room temperature.

C. Power-law blinking behavior

We found that the blinking behavior of DBOV for on and off times can be well fitted with power-law statistics in the short-time regime (times <~ 1.5 s, following from the lower photon count threshold of 5 photons/bin that is taken into account in the fitting). Representative fits at cryogenic temperature (91 K; 3.3 kW cm^{-2}) and room temperature (293 K; 3.3 kW cm^{-2}) are shown in Figs. 6(a), 6(b), 7(a), and 7(b), respectively. Linear fits to Eq. (2) on a log–log scale yield exponents α in the range of about −1.6 to −1.2, depending on the measurement condition. Within a dataset at fixed temperature and laser irradiance, the fitted exponent α values for t_{on} and t_{off} differ only moderately, with relative differences typically on the order of 5%–14% (median ≈9%). In comparison, the relative uncertainties of the fitted exponents are about 6%–14%

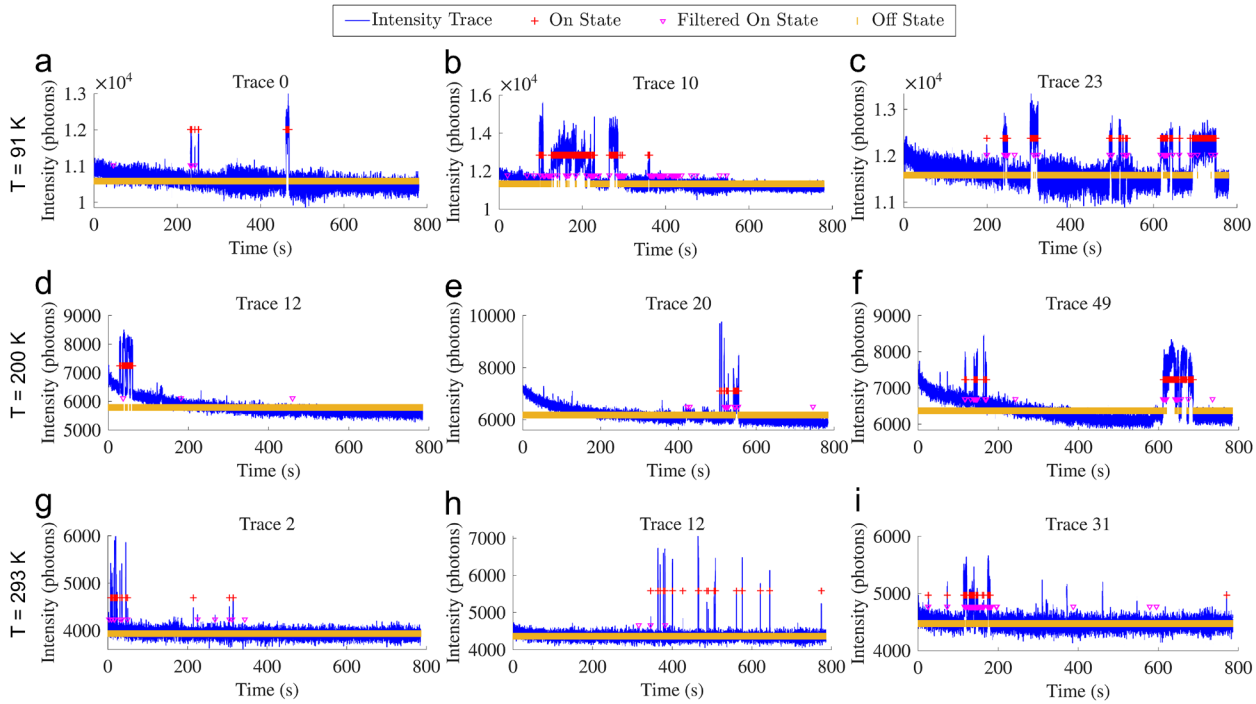

FIG. 5. Nine example intensity traces recorded at an excitation irradiance of 3.3 kW cm^{-2} (frame time 40 ms; intensity in photons per frame): [(a)–(c)], 91 K; [(d)–(f)], 200 K; and [(g)–(i)], 293 K. The red markers indicate frames classified as on-state by the GLRT. The orange band denotes the estimated background level. The magenta downward-pointing triangle markers indicate on-state frames that are excluded in the post-filtering step using the threshold $I_{\min}$. The three columns illustrate typical behaviors observed at each temperature: sparse activation (few on events), frequent activation (many on events), and intermediate behavior.

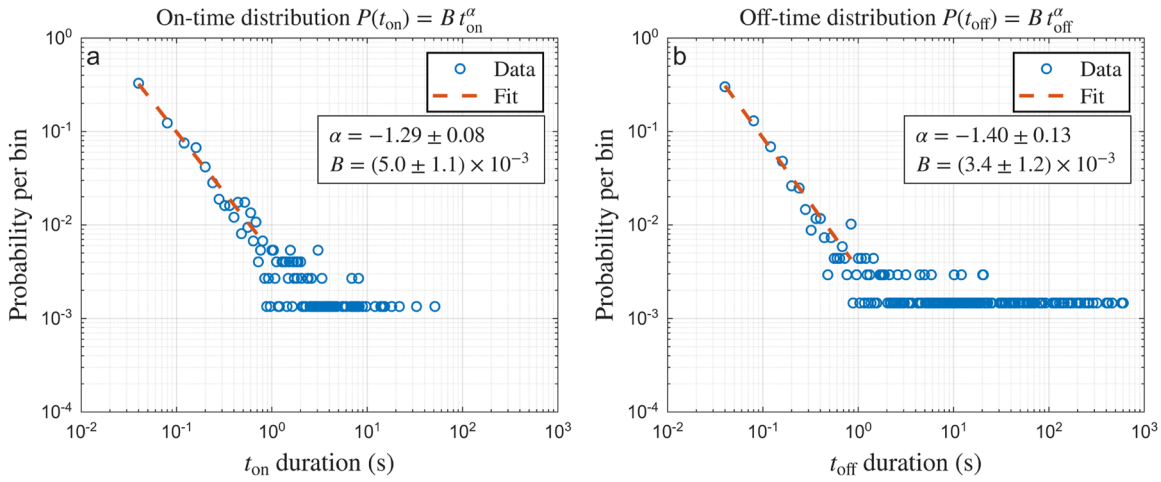

FIG. 6. Distributions of fluorescent blinking durations for on- and off-events measured at cryogenic temperatures (91 K) under 3.3 kW cm^{-2} excitation. The red dashed lines indicate power-law fits and are shown over the time extend that are used for the fitting. (a) Log–log histogram of on-time probability with power-law fit. (b) Log–log histogram of off-time probability with power-law fit.

(median ≈8%–9% for both t_{on} and t_{off}). The scaling prefactor B is not compared across datasets, as it can, in principle, be derived from the normalization of the (on or off) event probability distribution to one and, thus, depends on the minimum time (camera frame time) and maximum time (total measurement time). The major difference in the on and off time histograms is the occurrence of very long events (typically larger than about 1.5 s). In the on-time histograms, these rare events usually have a shorter duration than in the off-time

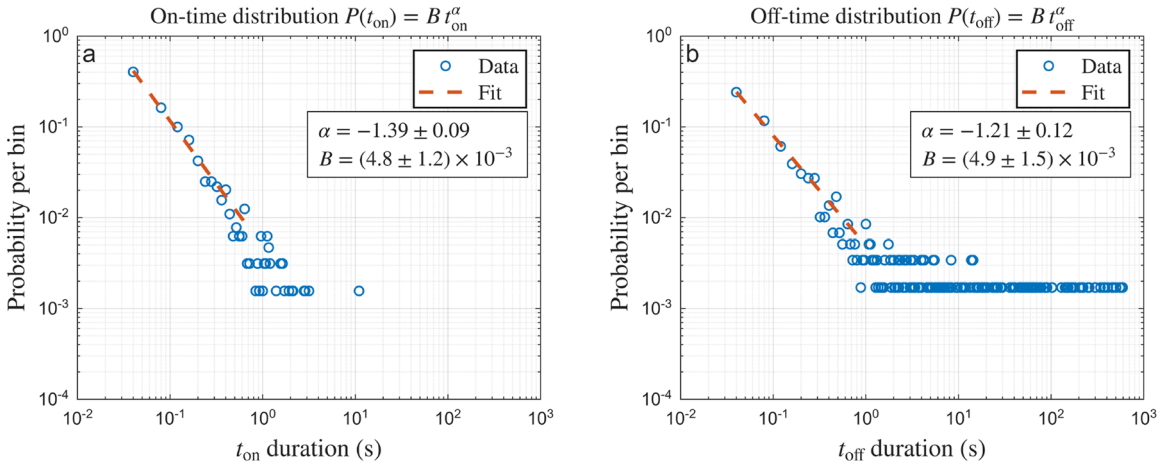

FIG. 7. Distributions of fluorescent blinking durations for on- and off-events measured at room temperature (293 K) under 3.3 kW cm^{-2} excitation. The red dashed lines indicate power-law fits and are shown over the time extend that are used for the fitting. (a) Log–log histogram of on-time probability with power-law fit. (b) Log–log histogram of off-time probability with power-law fit.

histograms. It is not clear if this long-time behavior can be fitted with a model like the power law behavior for the short-time behavior.

D. Dependence of blinking statistics on excitation irradiance

We investigated the blinking statistics as a function of excitation irradiance at cryogenic temperature (91 K) and at room temperature (293 K) and measured the dependence of the event-pooled and per-emitter mean on and off times as well as the short timescale power law exponent α. Additional power-law fits for all data points are provided in Figs. S1 and S2 of the supplementary material.

At cryogenic temperature, the event-pooled mean on-time $\langle t_{on}\rangle_{events}$ decreases with irradiance, whereas the event-pooled mean off-time $\langle t_{off}\rangle_{events}$ shows no significant trend [Fig. 8(a)]. The per-emitter mean on-time $\langle \bar{t}_{on}\rangle_{emitters}$ also decreases slightly with

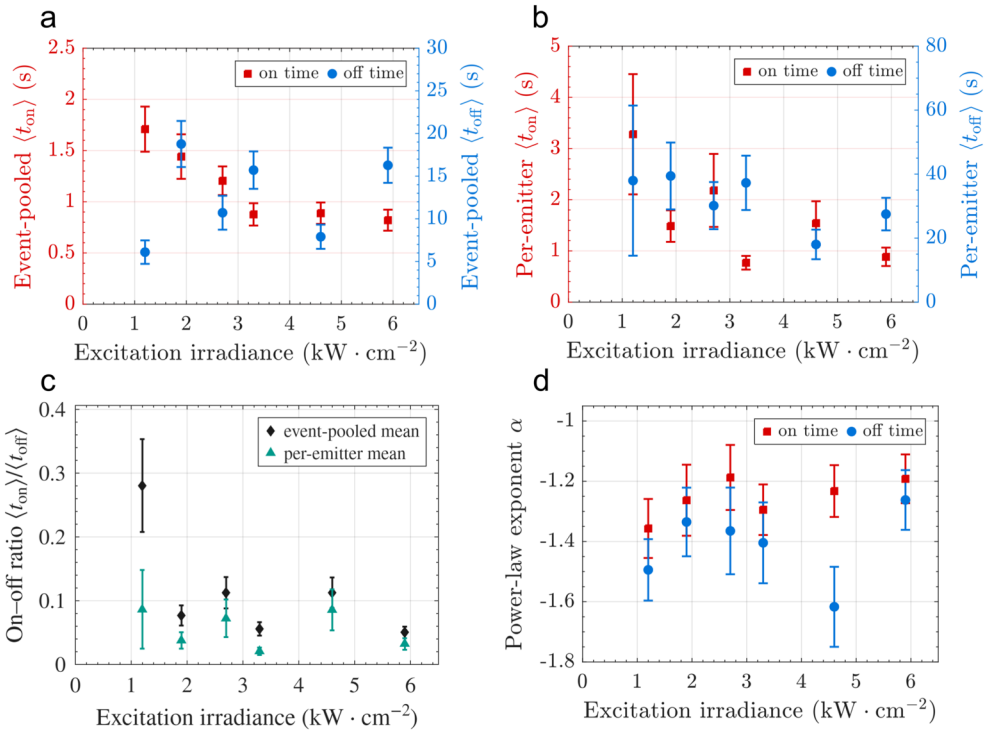

FIG. 8. Characterization of fluorescent blinking as a function of excitation irradiance at cryogenic temperature (91 K): (a) Event-pooled average on- and off-time durations. (b) Per-emitter average on- and off-time durations. (c) On–off time ratio. (d) Exponent α of the power-law fit.

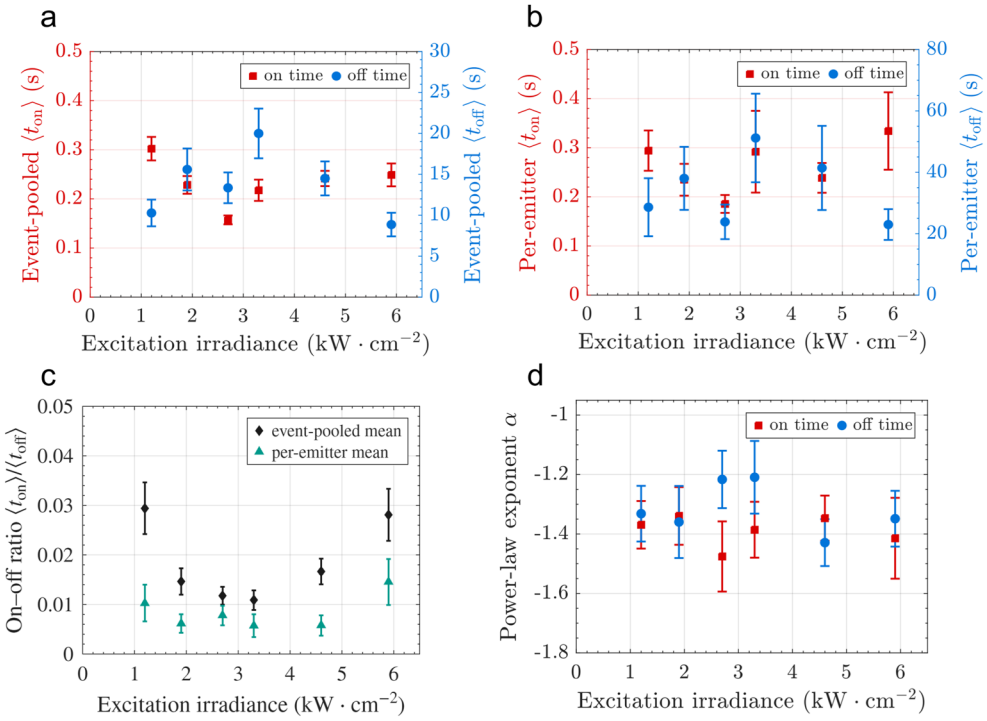

FIG. 9. Characterization of fluorescent blinking as a function of excitation irradiance on the sample at room temperature (293 K): (a) event-pooled average on- and off-time durations, (b) per-emitter average on- and off-time durations, (c) on–off time ratio, and (d) exponent α of the power-law fit.

irradiance, while the per-emitter mean off-time $\langle \bar{t}_{\mathrm{off}} \rangle_{\mathrm{emitters}}$ remains approximately constant in the range 20–40 s [Fig. 8(b)]. Consequently, the on–off ratio $r = \langle t_{\mathrm{on}} \rangle / \langle t_{\mathrm{off}} \rangle$ decreases with irradiance, from 0.28 ± 0.07 at the lowest tested irradiance (1.2 kW cm^{-2}) to 0.05 ± 0.01 at the highest (5.9 kW cm^{-2}) for the event-pooled ratio r_{events} and from 0.09 ± 0.06 to 0.03 ± 0.01 for the per-emitter ratio r_{emitters} [Fig. 8(d)]. The systematically smaller r_{emitters} compared to r_{events} reflects the fact that $\langle \bar{t}_{\mathrm{off}} \rangle_{\mathrm{emitters}}$ is roughly twice as large as $\langle t_{\mathrm{off}} \rangle_{\mathrm{events}}$. The power law exponent α for t_{on} is slightly but systematically larger (less negative) than that for t_{off} across the tested excitation irradiance range [Fig. 8(c)], indicating a steeper falloff toward longer event durations in the on-time statistics than in the off-time statistics. There does not seem to be a dependence on irradiance for the power law exponent.

At room temperature (293 K), the event-pooled mean on-time $\langle t_{\mathrm{on}} \rangle_{\mathrm{events}}$ remains nearly constant at about 0.23 s across the irradiance range, which is roughly five times shorter than the typical on time of 1.15 s at 91 K. A decrease in the mean on-time with irradiance is not apparent from the data. The per-emitter mean on-time $\langle \bar{t}_{\mathrm{on}} \rangle_{\mathrm{emitters}}$ similarly hovers at around 0.26 s [Figs. 9(a) and 9(b)], again about five times shorter than at 91 K. For the off-times, both the event-pooled mean $\langle t_{\mathrm{off}} \rangle_{\mathrm{events}}$ and the per-emitter mean $\langle \bar{t}_{\mathrm{off}} \rangle_{\mathrm{emitters}}$ show no clear monotonic trend with irradiance. A maximum for the middle of the measured range of irradiance values may be seen in the data. The found mean values remain in the range of 5–20 s (event pooled) and 20–50 s (per emitter), which is about the same level as for 91 K The on–off ratios r_{events} and r_{emitters} as functions of irradiance display a shallow minimum at 3.3 kW cm^{-2}, with values of 0.011 ± 0.002 and 0.006 ± 0.002, respectively, and slightly higher ratios at the lowest and highest irradiances [Fig. 9(d)]. The on–off ratios at 293 K are about one order of magnitude smaller than those at 91 K across the entire irradiance range, mainly because of the much smaller on-time at room temperature.

E. Dependence of blinking statistics on temperature

Next, we investigated the blinking statistics as a function of temperature at a fixed irradiance of 3.3 kW cm^{-2} and measured the dependence of the event-pooled and per-emitter mean on and off times, as well as the short timescale power law exponent α. Additional power-law fits for all data points are provided in Fig. S3 of the supplementary material.

Both the event-pooled mean on-time $\langle t_{\mathrm{on}} \rangle_{\mathrm{events}}$ and the per-emitter mean on-time $\langle \bar{t}_{\mathrm{on}} \rangle_{\mathrm{emitters}}$ decrease with temperature [Figs. 10(a) and 10(b)]. At cryogenic temperatures, the mean on-times are on the order of 1–1.5 s, whereas at room temperature, they are reduced to about 0.25 s, corresponding to an overall decrease by roughly a factor of 4–5. The two averaging schemes yield very similar temperature dependencies for t_{on}, indicating that emitter-to-emitter variability has a limited impact on the mean on-time over the temperature range studied. For the off-times, both the event-pooled mean $\langle t_{\mathrm{off}} \rangle_{\mathrm{events}}$ and the per-emitter mean $\langle \bar{t}_{\mathrm{off}} \rangle_{\mathrm{emitters}}$ show a shallow minimum at intermediate temperatures and larger values at the lowest and highest temperatures [Figs. 10(a) and 10(b)]. The per-emitter mean off-time decreases from 37.3 s at 93 K to 18.6 s at 150 K, stays around 18–22 s between 150 and 284 K, and then increases to 51.2 s at 293 K. The event-pooled means follow the same trend at smaller values. Thus, rather than a monotonic dependence, the mean off-time displays a broad minimum at intermediate temperatures with larger values at the cryogenic and room temperature ends. As a consequence, the on–off ratio $r = \langle t_{\mathrm{on}} \rangle / \langle t_{\mathrm{off}} \rangle$ decreases overall with temperature, but not strictly monotonically [Fig. 10(d)].

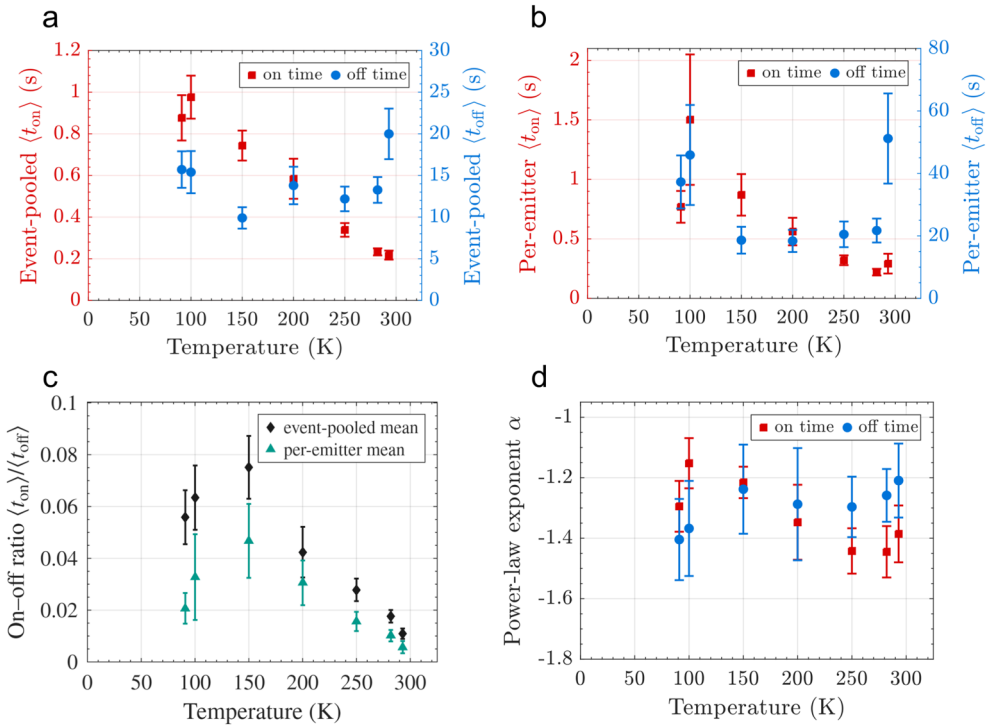

FIG. 10. Fluorescence blinking statistics as a function of temperature under 3.3 kW cm^{-2} excitation: (a) event-pooled average on- and off-time durations, (b) per-emitter average on- and off-time durations, (c) on–off time ratio, and (d) exponent α of the power-law fit.

The event-pooled ratio r_{events} increases slightly from 0.056 at 93 K to a maximum of 0.075 at 150 K and then decreases to 0.011 at 293 K, i.e., it is reduced by about a factor of five between 93 and 293 K. The per-emitter ratio r_{emitters} shows the same qualitative behavior, rising from 0.021 at 93 K to 0.047 at 150 K and then decreasing to 0.006 at 293 K (approximately a fourfold reduction between 93 and 293 K). Thus, both averaging schemes illustrate a pronounced reduction in the on–off ratio at room temperature compared to cryogenic temperature, with a modest peak in r around 150 K. The power-law exponents for t_{on} and t_{off} show only weak but opposite trends with temperature [Fig. 10(c)]. As the temperature is increased from 91 to 293 K, the exponent α for t_{on} varies between about −1.15 and −1.44 and tends to become more negative at higher temperatures, whereas the exponent for t_{off} varies between about −1.40 and −1.21 and tends to become less negative. The point-to-point variations are not strictly monotonic, but the overall tendencies are consistent with a slightly faster decay of the short-time t_{on} distribution and a slightly slower decay of the short-time t_{off} distribution as the temperature is raised.

F. Detected photon counts

We also quantified the number of foreground (signal) photons per frame and per on-event, as well as the background photon level, from the Gaussian fits in ROIs classified as on- or off-state by the GLRT (see Sec. II).

Figure 11 shows the fitted foreground photons as a function of excitation irradiance and temperature, while Fig. 12 shows the corresponding behavior of the background photons. At a given irradiance, the foreground photon output per on-frame is consistently higher at 91 K than at 293 K and increases with excitation irradiance for both temperatures [Fig. 11(a)]. Across the range of 1.2–5.9 kW cm^{-2}, the number of photons per on-frame at 91 K is larger than that at 293 K by a factor of ~2.0–2.7 (mean ~2.2). At 91 K, the per-frame foreground increases approximately linearly with irradiance (linear fit with $R^2 = 0.96$). At 293 K, a linear description is less adequate ($R^2 = 0.71$), and the two highest-irradiance points fall below the low-irradiance trend. The linear fits yield a non-zero intercept at zero irradiance, indicating a constant offset in the estimated per on-frame foreground. A fit-free estimate based on the background-subtracted ROI pixel sum yields photon counts lower by about a factor of two while preserving the qualitative trends, indicating that the offset is not caused by aspects of the PSF fitting but likely reflects a residual baseline contribution (e.g., stray light or back-scattered fluorescence). The photon yield per on-event shows weak variations with irradiance at a fixed temperature [Fig. 11(b)]. At 91 K, the foreground per on-event decreases with irradiance for the lower range of irradiance values and increases with irradiance for the higher range of irradiance values. At 293 K, no clear trend with excitation irradiance is observed. Figure 11(c) shows that the fitted foreground photons per on-event at constant excitation irradiance decreases with temperature, with an order of magnitude change over the measured temperature range (from about 3.1×10^4 to about 3.7×10^3).

The background photon count per pixel per frame, extracted from ROIs classified as off-state (GLRT, H_0), is plotted in Fig. 12. At both 91 and 293 K, the background increases with excitation irradiance and is systematically higher at 91 K than at 293 K [Fig. 12(a)], which follows a similar trend as the foreground signal per frame. At fixed irradiance, the background decreases with increasing

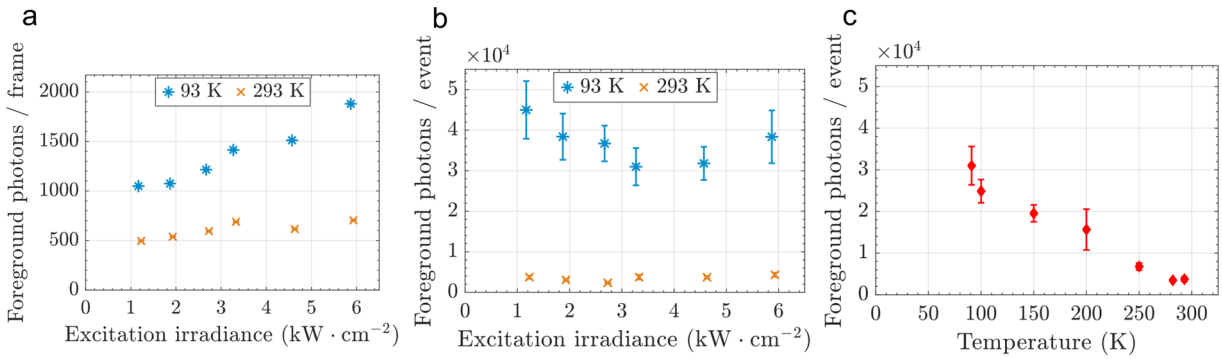

FIG. 11. Fitted foreground photon count per ROI (GLRT, H_1). (a) Foreground per on-frame as a function of excitation irradiance for 91 and 293 K. (b) Foreground per on-event as a function of excitation irradiance for 91 and 293 K. (c) Foreground per-on event as a function of temperature at fixed excitation irradiance of 3.3 kW cm^{-2}.

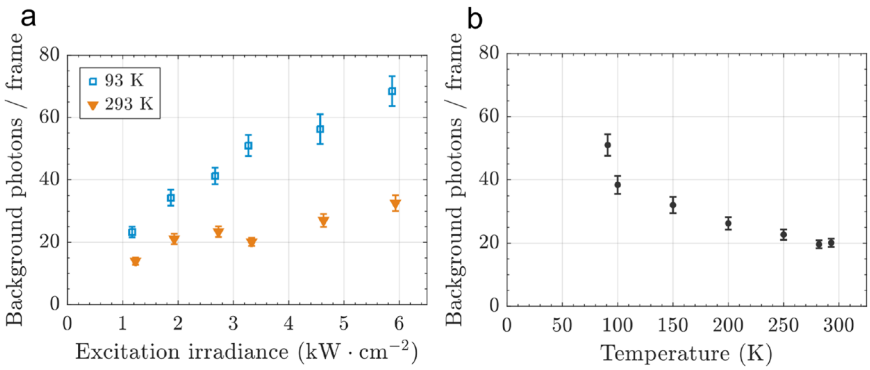

FIG. 12. Fitted averaged background photon count per frame per pixel (ROI 15 × 15 px, GLRT, H_0). Panel (a) shows background as a function of excitation irradiance for 91 and 293 K. Panel (b) shows background as a function of temperature at fixed excitation irradiance of 3.3 kW cm^{-2}.

temperature over the range of 91–293 K [Fig. 12(b)]. This clear temperature dependence indicates that the dominant source of background is not temperature-independent stray light or leakage of the excitation laser through the optics, but rather fluorescence from DBOV molecules. We attribute the background to emission from DBOV molecules that are out of focus or whose fluorescence is reflected by the highly reflective metal sample holder, so that this light is detected in a blurred, defocused manner on the camera.

IV. DISCUSSION AND CONCLUSIONS

In summary, we quantitatively characterized the blinking behavior and photon output of single DBOV-azide nanographene fluorophores between 91 and 293 K. Individual molecules exhibit intermittent blinking at all temperatures, with longer mean on-times and stronger frame-to-frame intensity fluctuations at cryogenic temperatures. In the short-time regime ($t < 1.5$ s), both on- and off-time distributions follow power-law statistics with exponents ranging between −1.6 and −1.2, without a systematic dependence on excitation irradiance or temperature within experimental uncertainty. At 91 K, mean on-times are shortened with increasing irradiance. Increasing temperature also shortens mean on-times and, more distinctly, reduces the on–off ratio by about an order of magnitude from 91 to 293 K. Per-emitter mean off-times are longer than event-pooled means, whereas the corresponding mean on-times are similar for both averaging schemes. As a result, per-emitter on–off ratios are generally smaller by a factor of 1.5–3; this points to heterogeneity of the nano-environment of the individual DBOV-azide molecules as a significant factor influencing blinking behavior. Finally, photons per on-frame, photons per on-event, and background photons per pixel display distinct dependencies on irradiance and temperature. Photon output and background are higher at cryogenic temperature, increase with irradiance, and decrease with temperature. The photon output per on-event is more independent of irradiance at 293 K but shows a non-monotonic dependence at 91 K.

Several limitations of the present study should be noted. First, due to the limitations of the cryostat, we investigated temperature dependence at only a single excitation irradiance and irradiance dependence at only one cryogenic (91 K) and one room (293 K) temperature. The full two-dimensional parameter space of irradiance and temperature remains unexplored. Second, the 40 ms camera exposure and finite recording time limit the accessible range of blinking times. In our measurements, the power-law behavior of both t_{on} and t_{off} extends from the camera frame time (40 ms) up to about 1.5 s. Beyond this range, very long events become too rare for reliable fitting. Consequently, the long-time tails of the on- and off-time distributions were not included in the power-law fits, even though these rare long events make a considerable contribution to the mean times, especially for the off times. This helps explain why the fitted exponents show no clear dependence on excitation irradiance or temperature, whereas the mean on-times and the on–off ratio still show some dependence on the experimental conditions,

in particular on temperature. Third, the background caused by the reflective metallic holder could be reduced by an improved design of the experimental setup. We can envision that the holder could be blackened and at the same time the cooling capacity of the setup increased, compensating the increased light absorption and thus heat load. Another possible solution would be to use a transmission-based cryo-setup where the sample can be mounted either on a TEM grid or on a cover glass and the excitation light only passes the sample once, e.g., a 4pi cryo microscope.[50] Finally, our analysis is phenomenological, relying on power-law fits and mean on/off times rather than on a full kinetic model, which limits the level of mechanistic interpretation.

At room temperature, the DBOV-azide blinking behavior reported here is qualitatively consistent with previous studies on DBOV derivatives, which found burst-like emission and heavy-tailed on-time statistics in polymer or glass matrices.[27–29] The short-time power-law statistics of both on- and off-times are in line with many previous reports on fluorescence intermittency in single emitters, including semiconductor quantum dots and organic dyes, where heavy-tailed on/off-time distributions with exponents typically in the range of about −1.2 to −1.8 are commonly observed.[35,36,51–54] The physical origin of such power-law intermittency has been widely discussed in the literature. Many models are based on charge separation and recombination, in which an electron or hole is transferred to one of many possible trap or acceptor sites in the environment and later returns by a recombination process with a broad distribution of time scales. Such charge–separation and recombination models naturally give rise to power-law-like on- and off-time statistics.[35,36,48,55] In these models, the power-law behavior of the on-states at the single-emitter level is linked to charge separation and recombination via tunneling to a dynamic distribution of charge acceptor sites in the local environment.[35] For DBOV-type nanographenes, recent work on DBOV-Mes (dibenzo[hi,st]ovalene with two mesityl groups) has proposed a photophysical model in which continuous excitation drives the molecules between a fluorescent neutral state and a long-lived, non-emissive radical cation formed by photoinduced ionization, while a near-infrared beam can reactivate fluorescence by photo-stimulated charge recombination.[56] The deactivation of DBOV denotes photoinduced ionization into the radical cation, and reactivation denotes recombination of this radical with an electron, which can occur spontaneously over time but is strongly enhanced by near-infrared photostimulation. This mechanism of cycling between a neutral emissive state and a charged dark state is conceptually similar to charge-separation and recombination models used to explain power-law blinking in dyes and quantum dots.[35,36,55] Our observation of power-law on- and off-time statistics together with a strong temperature dependence of the mean on times is consistent with DBOV-azide belonging to this class of charge-separation-based blinking mechanisms. In addition, at cryogenic temperatures, we observe a decrease in the on-time and of the foreground per on-event with increasing irradiance (at least for the smaller range of measured irradiance values), which is consistent with a two-photon process that drives the on-to-off transition. Our data, however, are not fully conclusive to firmly support the proposed model.

The found increase in photon yield at liquid-nitrogen temperatures is consistent with observations on other classes of fluorophores. Cryogenic experiments on fluorescent proteins and organic dyes typically report extended excited-state lifetimes, suppressed non-radiative relaxation, and strongly enhanced photon budgets per molecule compared to room temperature.[7–10] Our measurements on DBOV-azide follow this trend. Photons per on-frame at 91 K are roughly doubled compared to 293 K, while photons per on-event increase by about one order of magnitude, indicating that nanographene emitters also benefit from cryogenic operation in terms of brightness and usable photon budgets.

At the same time, we find that the on–off ratio at cryogenic temperature is substantially larger than at room temperature. The mean on–off ratio decreases with both increasing irradiance and increasing temperature, yet even under our most favorable conditions, the on–off ratio remains comparatively high. Similar behavior has been reported for photoactivatable and photoswitchable fluorescent proteins at cryogenic temperature, where freezing changes the fluorescent lifetimes and photoswitching kinetics and often leads to elevated on–off ratios.[14,15,17,20,21] For single-molecule localization microscopy, a high on–off ratio implies that many emitters in a diffraction-limited area are on simultaneously, increasing PSF overlap, limiting temporal separation of neighboring emitters, and thereby constraining the achievable localization density and resolution.[57] If the on–off ratio of DBOV-azide cannot be reduced by further optimization of the excitation scheme, sample environment, or chemical structure, then its application in cryo-SMLM is limited to cases with a relatively low labeling density. As a rule of thumb, an on/off ratio below 1/100 is needed for dense imaging of single molecules.[57,58] An alternative super-resolution microscope modality that exploits intensity fluctuations at high labeling densities is super-resolution optical fluctuation imaging (SOFI).[59] SOFI has been demonstrated previously under cryogenic conditions, enabling low-dose super-resolution fluorescence and correlative cryo-EM imaging.[60] DBOV-azide is currently an excellent candidate for SOFI type of imaging at cryogenic temperatures as its blinking properties match the requirements of SOFI. Here, long off times are not needed and simultaneous emission from many emitters is less problematic.[61]

On the methodological side, extending the present measurements to a broader range of irradiances and intermediate temperatures, acquiring higher-temporal-resolution data to track molecular pathways, and combining these experiments with explicit kinetic modeling of the on- and off-pathways could help identify the dominant thermally activated processes governing the on-to-off transition. Future studies may also entail time-resolved spectroscopy for a more direct test of the proposed ionization and recombination pathways.

Our approach to detect the (weak) single molecule fluorescence above the substantial background can be useful for other experiments where varying background levels or emitter brightness impairs the performance of simple approaches. Next to the sensitive GLRT,[42] we developed a criterion to reliably find all true positives with only little false positives. In situations where the integral signal photon count is, e.g., 500, we can tolerate 50 photons per pixel background, i.e., the total signal is about as strong as the noise in the footprint of the signal on the camera. Our code is openly available in a public GitLab repository.[30]

As to application in cryogenic fluorescence microscopy, our finding that DBOV-azide maintains intermittent blinking with

power-law distributed on- or off-times while exhibiting an elevated on–off ratio at cryogenic temperature suggests that nanographene emitters could be promising for SOFI under cryo-conditions, even if their blinking statistics are not ideal for conventional SMLM. The increased photon yield per on-event and per on-frame at 91 K compared to 293 K will be helpful to enable a good signal-to-noise ratio for such an application. A natural next step in this direction is to explore bio-conjugation strategies that link DBOV-azide or related DBOV derivatives to proteins, nucleic acids, or other biomolecular targets and to test their blinking and imaging performance on biological samples at cryogenic temperature, building on recent demonstrations of DBOV-based bioimaging in cellular and tissue contexts.[29] Such experiments would assess how the local environment in biological specimens influences the blinking statistics, photon yield, and on–off ratio and would clarify under which conditions DBOV-type nanographenes are practically applicable as cryogenic labels. Finally, integrating DBOV-azide into correlative light and electron microscopy may serve as a realistic test of whether the photophysical properties characterized here translate into practical benefits for imaging complex biological ultrastructure.

SUPPLEMENTARY MATERIAL

See the supplementary material for additional log–log on/off-time histograms and the corresponding power-law fits for all measurement conditions analyzed in this work.

ACKNOWLEDGMENTS

The authors acknowledge support from the European Research Council (ERC) (Advanced Grant, Grant Agreement No. 101055013, project Nanocubic). The authors thank Professor Akimitsu Narita and acknowledge his group at the Okinawa Institute of Science and Technology Graduate University (OIST), Japan, for the synthesis of the nanographene.

AUTHOR DECLARATIONS

Conflict of Interest

The authors have no conflicts to disclose.

Author Contributions

Yutong Wang: Conceptualization (supporting); Data curation (equal); Formal analysis (equal); Investigation (equal); Methodology (equal); Software (equal); Visualization (equal); Writing – original draft (equal); Writing – review & editing (equal). **Qiqi Yang**: Methodology (supporting); Resources (equal). **Xiaomin Liu**: Conceptualization (supporting); Resources (equal); Writing – review & editing (supporting). **Sjoerd Stallinga**: Conceptualization (equal); Formal analysis (equal); Funding acquisition (lead); Methodology (equal); Software (supporting); Supervision (equal); Writing – review & editing (equal). **Bernd Rieger**: Conceptualization (equal); Methodology (equal); Project administration (equal); Software (equal); Supervision (equal); Writing – review & editing (equal).

DATA AVAILABILITY

The data that support the findings of this study are openly available in the 4TU. ResearchData repository, http://doi.org/10.4121/3c67af67-b5d4-4b08-9a13-5bd888a91c45.

GLRT software for single-molecule on/off detection, implemented in MATLAB using DIPimage, is available in the GitLab repository at https://gitlab.tudelft.nl/imphys/ci/sm-onoff-glrt.

REFERENCES

[1] E. Betzig, G. H. Patterson, R. Sougrat, O. W. Lindwasser, S. Olenych, J. S. Bonifacino, M. W. Davidson, J. Lippincott-Schwartz, and H. F. Hess, "Imaging intracellular fluorescent proteins at nanometer resolution," Science **313**, 1642–1645 (2006).
[2] S. T. Hess, T. P. K. Girirajan, and M. D. Mason, "Ultra-high resolution imaging by fluorescence photoactivation localization microscopy," Biophys. J. **91**, 4258–4272 (2006).
[3] M. J. Rust, M. Bates, and X. Zhuang, "Sub-diffraction-limit imaging by stochastic optical reconstruction microscopy (STORM)," Nat. Methods **3**, 793–796 (2006).
[4] M. Heilemann, S. van de Linde, M. Schüttpelz, R. Kasper, B. Seefeldt, A. Mukherjee, P. Tinnefeld, and M. Sauer, "Subdiffraction-resolution fluorescence imaging with conventional fluorescent probes," Angew. Chem., Int. Ed. **47**, 6172–6176 (2008).
[5] R. J. Ober, S. Ram, and E. S. Ward, "Localization accuracy in single-molecule microscopy," Biophys. J. **86**, 1185–1200 (2004).
[6] W. Li, S. C. Stein, I. Gregor, and J. Enderlein, "Ultra-stable and versatile widefield cryo-fluorescence microscope for single-molecule localization with sub-nanometer accuracy," Opt. Express **23**, 3770–3783 (2015).
[7] C. N. Hulleman, W. Li, I. Gregor, B. Rieger, and J. Enderlein, "Photon yield enhancement of red fluorophores at cryogenic temperatures," ChemPhysChem **19**, 1774–1780 (2018).
[8] H. Mazal, F.-F. Wieser, and V. Sandoghdar, "Insights into protein structure using cryogenic light microscopy," Biochem. Soc. Trans. **51**, 2041–2059 (2023).
[9] S. Adhikari, R. Smit, and M. Orrit, "Future paths in cryogenic single-molecule fluorescence spectroscopy," J. Phys. Chem. C **128**, 3–18 (2024).
[10] P. D. Dahlberg and W. E. Moerner, "Cryogenic super-resolution fluorescence and electron microscopy correlated at the nanoscale," Annu. Rev. Phys. Chem. **72**, 253–278 (2021).
[11] J. Dubochet, "The physics of rapid cooling and its implications for cryoimmobilization of cells," in *Methods in Cell Biology*, *Cellular Electron Microscopy* (Academic Press, 2007), Vol. 79, pp. 7–21.
[12] C. L. Schwartz, V. I. Sarbash, F. I. Ataullakhanov, J. R. Mcintosh, and D. Nicastro, "Cryo-fluorescence microscopy facilitates correlations between light and cryo-electron microscopy and reduces the rate of photobleaching," J. Microsc. **227**, 98–109 (2007).
[13] D. P. Hoffman, G. Shtengel, C. S. Xu, K. R. Campbell, M. Freeman, L. Wang, D. E. Milkie, H. A. Pasolli, N. Iyer, J. A. Bogovic, D. R. Stabley, A. Shirinifard, S. Pang, D. Peale, K. Schaefer, W. Pomp, C.-L. Chang, J. Lippincott-Schwartz, T. Kirchhausen, D. J. Solecki, E. Betzig, and H. F. Hess, "Correlative three-dimensional super-resolution and block-face electron microscopy of whole vitreously frozen cells," Science **367**, eaaz5357 (2020).
[14] M. W. Tuijtel, A. J. Koster, S. Jakobs, F. G. A. Faas, and T. H. Sharp, "Correlative cryo super-resolution light and electron microscopy on mammalian cells using fluorescent proteins," Sci. Rep. **9**, 1369 (2019).
[15] P. D. Dahlberg, S. Saurabh, A. M. Sartor, J. Wang, P. G. Mitchell, W. Chiu, L. Shapiro, and W. E. Moerner, "Cryogenic single-molecule fluorescence annotations for electron tomography reveal in situ organization of key proteins in *Caulobacter*," Proc. Natl. Acad. Sci. U. S. A. **117**, 13937–13944 (2020).
[16] R. Kaufmann, C. Hagen, and K. Grünewald, "Fluorescence cryo-microscopy: Current challenges and prospects," Curr. Opin. Chem. Biol. Mol. Imaging **20**, 86–91 (2014).
[17] Y.-W. Chang, S. Chen, E. I. Tocheva, A. Treuner-Lange, S. Löbach, L. Søgaard-Andersen, and G. J. Jensen, "Correlated cryogenic photoactivated localization microscopy and cryo-electron tomography," Nat. Methods **11**, 737–739 (2014).

[18]D. B. Boltje, J. P. Hoogenboom, A. J. Jakobi, G. J. Jensen, C. T. Jonker, M. J. Kaag, A. J. Koster, M. G. Last, C. de Agrela Pinto, J. M. Plitzko, S. Raunser, S. Tacke, Z. Wang, E. B. van der Wee, R. Wepf, and S. den Hoedt, "A cryogenic, coincident fluorescence, electron, and ion beam microscope," eLife **11**, e82891 (2022).
[19]E. G. Perton, D. B. Boltje, A. J. Jakobi, and J. P. Hoogenboom, "Workflow for fluorescence-targeted lamella milling from vitrified cells with a coincident fluorescence, electron, and ion beam microscope," Bio-Protoc. **15**, e5390 (2025).
[20]A. M. Sartor, P. D. Dahlberg, D. Perez, and W. E. Moerner, "Characterization of mApple as a red fluorescent protein for cryogenic single-molecule imaging with turn-off and turn-on active control mechanisms," J. Phys. Chem. B **127**, 2690–2700 (2023).
[21]D. Perez, D. P. Dowlatshahi, C. A. Azaldegui, T. B. Ansell, P. D. Dahlberg, and W. E. Moerner, "Exploring transient states of PAmKate to enable improved cryogenic single-molecule imaging," J. Am. Chem. Soc. **146**, 28707–28716 (2024).
[22]C. N. Hulleman, M. Huisman, R. J. Moerland, D. Grünwald, S. Stallinga, and B. Rieger, "Fluorescence polarization control for on–off switching of single molecules at cryogenic temperatures," Small Methods **2**, 1700323 (2018).
[23]C. N. Hulleman, R. J. Moerland, S. Stallinga, and B. Rieger, "Polarized stimulated-emission depletion and dark-state lifetime at vacuum and cryogenic temperature conditions," Phys. Rev. A **104**, 063516 (2021).
[24]D. Böning, F.-F. Wieser, and V. Sandoghdar, "Polarization-encoded colocalization microscopy at cryogenic temperatures," ACS Photonics **8**, 194–201 (2021).
[25]H. Mazal, F.-F. Wieser, and V. Sandoghdar, "Deciphering a hexameric protein complex with Angstrom optical resolution," eLife **11**, e76308 (2022).
[26]Q. Li, C. N. Hulleman, R. J. Moerland, E. Mailvaganam, S. Ganapathy, D. Brinks, S. Stallinga, and B. Rieger, "Waveguide-based total internal reflection fluorescence microscope enabling cellular imaging under cryogenic conditions," Opt. Express **29**, 34097–34108 (2021).
[27]X. Liu, S.-Y. Chen, Q. Chen, X. Yao, M. Gelléri, S. Ritz, S. Kumar, C. Cremer, K. Landfester, K. Müllen, S. H. Parekh, A. Narita, and M. Bonn, "Nanographenes: Ultrastable, switchable, and bright probes for super-resolution microscopy," Angew. Chem., Int. Ed. **59**, 496–502 (2020).
[28]E. Jin, Q. Yang, C.-W. Ju, Q. Chen, K. Landfester, M. Bonn, K. Müllen, X. Liu, and A. Narita, "A highly luminescent nitrogen-doped nanographene as an acid- and metal-sensitive fluorophore for optical imaging," J. Am. Chem. Soc. **143**, 10403–10412 (2021).
[29]X. Zhu, Q. Chen, H. Zhao, Q. Yang, Goudappagouda, M. Gelléri, S. Ritz, D. Ng, K. Koynov, S. H. Parekh, V. K. Chetty, B. K. Thakur, C. Cremer, K. Landfester, K. Müllen, M. Terenzio, M. Bonn, A. Narita, and X. Liu, "Intrinsic burst-blinking nanographenes for super-resolution bioimaging," J. Am. Chem. Soc. **146**, 5195–5203 (2024).
[30]Y. Wang, S. Stallinga, and B. Rieger, "GLRT-based single-molecule on-off detection," GitLab repository, Apache License 2.0 (2026); https://gitlab.tudelft.nl/imphys/ci/sm-onoff-glrt.
[31]R. Heintzmann, P. K. Relich, R. P. J. Nieuwenhuizen, K. A. Lidke, and B. Rieger, "Calibrating photon counts from a single image," arXiv:1611.05654 [physics] (2018).
[32]C. S. Smith, N. Joseph, B. Rieger, and K. A. Lidke, "Fast, single-molecule localization that achieves theoretically minimum uncertainty," Nat. Methods **7**, 373–375 (2010).
[33]S. Stallinga and B. Rieger, "Accuracy of the Gaussian point spread function model in 2D localization microscopy," Opt. Express **18**, 24461–24476 (2010).
[34]G. T. Dempsey, J. C. Vaughan, K. H. Chen, M. Bates, and X. Zhuang, "Evaluation of fluorophores for optimal performance in localization-based super-resolution imaging," Nat. Methods **8**, 1027–1036 (2011).
[35]J. P. Hoogenboom, J. Hernando, E. M. H. P. van Dijk, N. F. van Hulst, and M. F. García-Parajó, "Power-law blinking in the fluorescence of single organic molecules," ChemPhysChem **8**, 823–833 (2007).
[36]M. Haase, C. G. Hübner, E. Reuther, A. Herrmann, K. Müllen, and Th. Basché, "Exponential and power-law kinetics in single-molecule fluorescence intermittency," J. Phys. Chem. B **108**, 10445–10450 (2004).
[37]M. Lippitz, F. Kulzer, and M. Orrit, "Statistical evaluation of single nano-object fluorescence," ChemPhysChem **6**, 770–789 (2005).
[38]L. P. Watkins and H. Yang, "Detection of intensity change points in time-resolved single-molecule measurements," J. Phys. Chem. B **109**, 617–628 (2005).
[39]R. Killick, P. Fearnhead, and I. A. Eckley, "Optimal detection of changepoints with a linear computational cost," J. Am. Stat. Assoc. **107**, 1590–1598 (2012).
[40]L. Loeff, J. W. J. Kerssemakers, C. Joo, and C. Dekker, "*AutoStepfinder*: A fast and automated step detection method for single-molecule analysis," Patterns **2**, 100256 (2021).
[41]I. M. Palstra and A. F. Koenderink, "A Python toolbox for unbiased statistical analysis of fluorescence intermittency of multilevel emitters," J. Phys. Chem. C **125**, 12050–12060 (2021).
[42]C. S. Smith, S. Stallinga, K. A. Lidke, B. Rieger, and D. Grunwald, "Probability-based particle detection that enables threshold-free and robust in vivo single-molecule tracking," Mol. Biol. Cell **26**, 4057–4062 (2015).
[43]K. J. A. Martens, A. N. Bader, S. Baas, B. Rieger, and J. Hohlbein, "Phasor based single-molecule localization microscopy in 3D (pSMLM-3D): An algorithm for MHz localization rates using standard CPUs," J. Chem. Phys. **148**, 123311 (2017).
[44]R. Ø. Thorsen, C. N. Hulleman, M. Hammer, D. Grünwald, S. Stallinga, and B. Rieger, "Impact of optical aberrations on axial position determination by photometry," Nat. Methods **15**, 989–990 (2018).
[45]Y. Benjamini and D. Yekutieli, "The control of the false discovery rate in multiple testing under dependency," Ann. Stat. **29**, 1165–1188 (2001).
[46]D. Chicco and G. Jurman, "The advantages of the Matthews correlation coefficient (MCC) over F1 score and accuracy in binary classification evaluation," BMC Genomics **21**, 6 (2020).
[47]A. C. Davison and D. V. Hinkley, *Bootstrap Methods and their Application* (Cambridge University Press, 1997).
[48]P. A. Frantsuzov, S. Volkán-Kacsó, and B. Jankó, "Universality of the fluorescence intermittency in nanoscale systems: Experiment and theory," Nano Lett. **13**, 402–408 (2013).
[49]P. A. Frantsuzov, S. Volkán-Kacsó, and B. Jankó, "Model of fluorescence intermittency of single colloidal semiconductor quantum dots using multiple recombination centers," Phys. Rev. Lett. **103**, 207402 (2009).
[50]Q. Li, "Cryogenic 4Pi single molecule localization microscopy," Ph.D. thesis, Delft University of Technology, Delft, 2025.
[51]M. Kuno, D. P. Fromm, H. F. Hamann, A. Gallagher, and D. J. Nesbitt, "'On'/'off' fluorescence intermittency of single semiconductor quantum dots," J. Chem. Phys. **115**, 1028–1040 (2001).
[52]D. S. Lidke, P. Nagy, R. Heintzmann, D. J. Arndt-Jovin, J. N. Post, H. E. Grecco, E. A. Jares-Erijman, and T. M. Jovin, "Quantum dot ligands provide new insights into erbB/HER receptor–mediated signal transduction," Nat. Biotechnol. **22**, 198–203 (2004).
[53]K. A. Lidke, B. Rieger, T. M. Jovin, and R. Heintzmann, "Superresolution by localization of quantum dots using blinking statistics," Opt. Express **13**, 7052–7062 (2005).
[54]R. Schmidt, C. Krasselt, C. Göhler, and C. von Borczyskowski, "The fluorescence intermittency for quantum dots is not power-law distributed: A luminescence intensity resolved approach," ACS Nano **8**, 3506–3521 (2014).
[55]F. Cichos, C. von Borczyskowski, and M. Orrit, "Power-law intermittency of single emitters," Curr. Opin. Colloid Interface Sci. **12**, 272–284 (2007).
[56]Q. Yang, A. V. Failla, P. Turunen, A. Mateos-Maroto, M. Gai, W. Zuschratter, S. Westendorf, M. Gelléri, Q. Chen, Goudappagouda, H. Zhao, X. Zhu, S. Morsbach, M. Scheele, W. Yan, K. Landfester, R. Kabe, M. Bonn, A. Narita, and X. Liu, "Reactivatable stimulated emission depletion microscopy using fluorescence-recoverable nanographene," Nat. Commun. **16**, 1341 (2025).
[57]A. R. Small, "Theoretical limits on errors and acquisition rates in localizing switchable fluorophores," Biophys. J. **96**, L16–L18 (2009).
[58]R. P. J. Nieuwenhuizen, K. A. Lidke, M. Bates, D. L. Puig, D. Grünwald, S. Stallinga, and B. Rieger, "Measuring image resolution in optical nanoscopy," Nat. Methods **10**, 557–562 (2013).

[59]T. Dertinger, R. Colyer, G. Iyer, S. Weiss, and J. Enderlein, "Fast, background-free, 3D super-resolution optical fluctuation imaging (SOFI)," Proc. Natl. Acad. Sci. U. S. A. **106**, 22287–22292 (2009).
[60]F. Moser, V. Pražák, V. Mordhorst, D. M. Andrade, L. A. Baker, C. Hagen, K. Grünewald, and R. Kaufmann, "Cryo-SOFI enabling low-dose super-resolution correlative light and electron cryo-microscopy," Proc. Natl. Acad. Sci. U. S. A. **116**, 4804–4809 (2019).
[61]B. Moeyaert, W. Vandenberg, and P. Dedecker, "SOFIevaluator: A strategy for the quantitative quality assessment of SOFI data," Biomed. Opt. Express **11**, 636 (2020).